CrossMark

DNS Study of Dust Particle Resuspension in a Fusion Reactor Induced by a Transonic Jet into Vacuum

Gabriele Camerlengo[1] (ID) · Domenico Borello[2] ·
Alessandro Salvagni[2] · Jörn Sesterhenn[1]

Abstract This paper reports on a two-phase flow Direct Numerical Simulation (DNS) aimed at analyzing the resuspension of solid particles from a surface hit by a transonic jet inside a low pressure container. Conditions similar to those occurring in a fusion reactor vacuum vessel during a Loss of Vacuum Accident (LOVA) have been considered. Indeed, a deep understanding of the resuspension phenomenon is essential to make those reactors safe and suitable for a large-scale sustainable energy production. The jet Reynolds and Mach numbers are respectively set to 3300 and 1. The Thornton and Ning impact/adhesion model is adopted and improved. An advanced resuspension model, which takes into account the dynamics (rolling and slipping) of particles at the wall, is implemented. The use of this model combined with a DNS represents a great novelty in simulating the particle resuspension process. The particles initially deposited at the wall have constant density, whereas their diameters are drawn according to a log-normal distribution, with parameters obtained from experimental data. It has been found that the flow induced motion of wall deposited particles

---

✉ Gabriele Camerlengo
gabriele.camerlengo@tu-berlin.de

Domenico Borello
domenico.borello@uniroma1.it

Alessandro Salvagni
alessandro.salvagni@uniroma1.it

Jörn Sesterhenn
joern.sesterhenn@tu-berlin.de

[1] Institut für Strömungsmechanik und Technische Akustik, Technische Universität Berlin,
Müller-Breslau-Str. 15, 10623 Berlin, Germany

[2] Dipartimento di Ingegneria Meccanica e Aerospaziale, Università degli Studi di Roma "La
Sapienza", Via Eudossiana 18, 00184 Roma, Italy

is highly linked with the instantaneous fluid structures and the resuspension phenomenon predominantly affects particles with the largest diameters. Moreover, the jet-deposit interaction is mostly confined within a circumference around the jet of radius approximately equal to the jet diameter.

1 Introduction

In fluid dynamics, resuspension refers to the process by which particles, previously airborne and then deposited on a surface, are removed and picked up under the action of a flow. This phenomenon occurs widely both in nature and industry: it is a matter of concern in environment, soil and forensic science, filtration technology, chemistry, biology, sedimentology and energy industry [1].

Although early studies assumed that the balance between adhesion and lift forces was the main resuspension trigger [2], it is now well established that a deposited particle is firstly set in motion on the surface under the action of aerodynamic forces (mainly drag). Subsequently, it is assumed that the lift force is sufficient to break the particle-wall adhesion when a moving particle crashes into an asperity. From this perspective a first class of models [3] regards a particle as being resuspended as the static balance of forces (and torques) acting on it becomes non-zero. Among them, the most advanced studies include the surface roughness influence on the adhesion force, which has been demonstrated to play a decisive role on the resuspension phenomenon. Nevertheless, the key issue of the static force balance approach is assuming all the forces at play known, and notably they consider average aerodynamic forces originating from the average flow field [4]. These models are then approximate, since the influence of turbulent bursts is not directly taken into account. A second type of model, based on the energy accumulation approach, compares the vibrational energy of a deposited particle with the work required to break the adhesive contact with the surface [5]. This approach, also referred to as quasi-static approach, represents an improvement with respect to the static one, since the energy transfer from the turbulent structures to the deposited particles is now considered. Recently a new class of models, which take into account the entire dynamics of the particles at the wall (rolling and slipping), has been introduced [6]. Whereas the former models are based on the conservative approximation by which the resuspension event is confused with the first detachment occurence, the dynamic models see the resuspension as the consequence of the interaction between the particle motion on the surface and the surface asperities.

In this paper the resuspension phenomenon is investigated addressing its relevance in ensuring the fusion reactors safety, which constitutes one of the major obstacles to make them operative and provide us with abundant, clean and CO_2 free energy. Specifically, one of the main safety issue of those reactors is related to the plasma which is highly aggressive and erodes the containing vessel such that radioactive metal dust particles continuously pile up at the bottom. Since the reactor operates at a pressure of about 50 mbar, if a leak in the vessel occurs, a transonic turbulent jet stirs up the dust and a radioactive hazard, so called Loss of Vacuum Accident (LOVA), is imminent [7]. Therefore, we present the interaction of a transonic jet with heavy dust particles deposited at the wall using a dynamic resuspension model combined with an improved Thornton and Ning impact/adhesion model. In this context few RANS and LES studies, primarily aimed at reconstructing the flow field during the

course of a LOVA, exist [8, 9]. Thus, it is expected that the present Direct Numerical Simulation will bring a great advance in understanding the physics of the phenomenon under the underlined operative conditions.

2 Mathematical Modeling

In the present work, particles (i.e. the dispersed phase) are modeled as solid spheres and described in the Lagrangian specification, whilst the flow field (i.e. the continuous phase) is solved using the Eulerian specification. A two-way coupling method is used, so that both the dispersed-to-continuous and continuous-to-dispersed phase force transfer is considered. A 1st order polynomial interpolation is employed to compute the fluid proprieties at the particle positions. In the next sections, the adopted models are presented as concerns both the simulated phases.

2.1 Fluid transport

The compressible Navier-Stokes equations are solved in a characteristic pressure-velocity-entropy formulation introduced by Sesterhenn [10]. This formulation offers several advantages in the implementation of boundary conditions and provides additional numerical stability by allowing the use of upwind schemes without losing accuracy.

As concerns the space discretization, a 6th order compact central scheme is used for the diffusive term, whereas a 5th order upwind scheme is employed for the convective term. The time integration is performed through a 4th order Runge-Kutta method. Because of the occurrence of weak shocks in the flow, a 2nd order shock-capturing filter is also implemented in order to prevent numerical instabilities [11].

2.2 Particle transport

The particle transport equation is derived from the general one presented by Elghobashi [12], under the assumption that the ratio fluid density to particle density is much smaller than one, i.e. $\rho_f/\rho_p \ll 1$. One obtains for a generic particle:

$$\frac{dv}{dt} = \frac{u - v}{\tau_p} + \frac{F_L}{\rho_p} + \frac{3}{2}\frac{\rho_f}{\rho_p}\frac{Du}{Dt} + g \tag{1}$$

with v and u respectively the particle and fluid velocity vectors, F_L the particle lift force and g the gravity force per unit mass. The quantity τ_p, known as particle relaxation time, represents the exponential time constant of the particle velocity decay in a quiescent fluid. It is given by:

$$\tau_p = \frac{4}{3}\frac{\rho_p d_p^2}{\mu_f C_D \mathrm{Re}_p} \tag{2}$$

with μ_f the dynamic viscosity of the fluid, C_D the particle drag coefficient, d_p the particle diameter and Re_p the particle Reynolds number, which is defined as:

$$\mathrm{Re}_p = \frac{d_p V_{rel}}{\nu_f} \tag{3}$$

with $\nu_f = \mu_f/\rho_f$ the kinematic viscosity of the fluid and V_{rel} the magnitude of the particle-fluid relative velocity vector, i.e.:
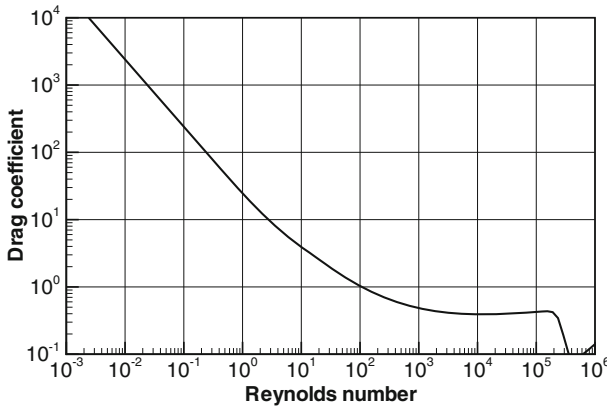
$$V_{rel} = \|u - v\|. \tag{4}$$

Fig. 1 Drag coefficient for flow around a sphere as a function of the Reynolds number [13]

In Fig. 1 the drag coefficient for spherical particles as a function of the particle Reynolds number is shown [13]. Since typical particle Reynolds numbers are much less than 800 the Schiller-Naumann correlation [14] can be used:

$$C_D = \frac{24}{\mathrm{Re}_p} \left(1 + 0.15\mathrm{Re}_p^{0.687}\right) \qquad \mathrm{Re}_p \leq 800. \tag{5}$$

As regards the lift force $\boldsymbol{F_L}$, the one-dimensional formulation by Cherukat and McLaughlin [15] for spherical particles near a wall is considered:

$$\boldsymbol{F_L} = \frac{1}{4}\rho_f d_p^2 V_{rel} I_L \,\hat{\mathbf{n}} \tag{6}$$

where $\hat{\mathbf{n}}$ is the unit normal vector to the wall and I_L is equal to:

$$
\begin{aligned}
I_L = {}& \left(1.7631 + 0.3561\kappa - 1.1837\kappa^2 + 0.845163\kappa^3\right) \\
& - \left(\frac{3.24139}{\kappa} + 2.6760 + 0.8248\kappa - 0.4616\kappa^2\right)\Lambda_g \\
& + \left(1.8081 + 0.879585\kappa - 1.9009\kappa^2 + 0.98149\kappa^3\right)\Lambda_g^2.
\end{aligned}
\tag{7}
$$

The parameter κ and the non-dimensional shear rate Λ_g are given by:

$$\kappa = \frac{d_p}{2y} \qquad \text{and} \qquad \Lambda_g = \frac{d_p}{2V_{rel}}G \tag{8}$$

with y the distance of the particle center from the wall and G the shear rate in the main direction of the flow.

The two-way coupling is accomplished by distributing the force acting on every particle to the surrounding fluid, according to the weighting functions used for the interpolation of the flow field in the particle positions. To this end, the traditional right-hand side RHS of the Navier-Stokes momentum equations in the n-th grid point and i-th direction is updated into:

$$\mathrm{RHS}'_{n,i} = \mathrm{RHS}_{n,i} + \sum_{k=1}^{N_p} G_{n,k} F_{k,i} \tag{9}$$

with N_p the total number of computed particles, $F_{k,i}$ the total force exerted by the k-th particle on the fluid and $G_{n,k}$ the corresponding weighting function, i.e. the fraction of the force ascribed to the n-th grid point.

2.3 Particle-wall impact

Regarding the particle-wall impact model, a generalized version of the Thornton and Ning model [16] is implemented to reproduce the elasto-plastic behavior of an airborne particle when it impacts the wall. The upgraded model here presented removes the Thornton and Ning's original hypothesis that a particle may stick on the wall only when the collision is elastic.

Let us examine a first stage of the collision where only plastic deformation effects are taken into account. A restitution coefficient e_0 considering uniquely the energy loss due to the plastic deformation may be then defined as [16]:

$$
e_0 = \sqrt{\frac{2E_0}{m_p v_i^2}} =
\begin{cases}
1 & v_i \leq v_y, \\
\left(\frac{6\sqrt{3}}{5}\right)^{1/2} \left[1 - \frac{1}{6}\left(\frac{v_y}{v_i}\right)^2\right]^{1/2} \\
\quad \times \left[\dfrac{\dfrac{v_y}{v_i}}{\dfrac{v_y}{v_i} + 2\sqrt{\dfrac{6}{5} - \dfrac{1}{5}\left(\dfrac{v_y}{v_i}\right)^2}}\right]^{1/4} & v_i > v_y
\end{cases}
\tag{10}
$$

with E_0 the particle remaining kinetic energy after the impact, m_p the particle mass, v_i the normal impact velocity and v_y (yield velocity) the minimum velocity above which the plastic deformations take place. It is given by:

$$
v_y = \left(\frac{\pi}{2E^*}\right)^2 \left(\frac{2}{5\rho_p}\right)^{1/2} p_y^{5/2}
\tag{11}
$$

where p_y is the particle yield pressure,[1] which can be estimated as 1.6 times the yield strength of the material, [17] and E^* the equivalent Young's modulus which depends on the properties of the two bodies in contact (particle and wall), namely:

$$
E^* = \left(\frac{1 - v_1^2}{E_1} + \frac{1 - v_2^2}{E_2}\right)^{-1}
\tag{12}
$$

with E_i the Young's moduli and v_i the Poisson's ratios ($i = 1, 2$).

At a second stage the particle bounces provided that its remaining kinetic energy is greater than the work needed to break the contact. The latter is given by Thornton and Ning for a sphere of radius R_p impacting a flat surface as:

$$
W_s = 7.09 \left(\frac{\Gamma^5 R_p^4}{E^{*2}}\right)^{1/3}
\tag{13}
$$

---

[1]In the process of collision the yield pressure is reached at the center of the two bodies contact area when the plastic deformation attains the contact surface at its perimeter.

with Γ the adhesion energy of the interface. The bounce occurrence condition can be written as:

$$E_0 = \frac{1}{2}m_p\,(e_0 v_i)^2 > W_s \tag{14}$$

which leads to the definition of the sticking velocity, i.e. the minimum normal impact velocity necessary for a bounce to happen, namely:

$$v_s = \frac{1}{e_0}\left(\frac{2W_s}{m_p}\right)^{1/2} = \frac{1.84}{e_0}\left[\frac{(\Gamma/R_p)^5}{\rho_p^3 E^{*2}}\right]^{1/6}. \tag{15}$$

If Eq. 14 holds, the residual particle kinetic energy is:

$$\frac{1}{2}m_p v_f^2 = \frac{1}{2}m_p\,(e_0 v_i)^2 - W_s = \frac{1}{2}m_p e_0^2\left(v_i^2 - v_s^2\right) \tag{16}$$

with v_f the normal velocity of the particle after the impact. Hence the final expression of the restitution coefficient ($e = v_f/v_i$) is provided by:

$$e = \begin{cases} 0 & v_i \leq v_s, \\[2mm] e_0\left[1 - \left(\dfrac{v_s}{v_i}\right)^2\right]^{1/2} & v_i > v_s. \end{cases} \tag{17}$$

In Fig. 2 the restitution coefficient is plotted against the normalized normal impact velocity (v_i/v_y) for different values of v_s'/v_y, being $v_s' = (2W_s/m_p)^{1/2}$ the sticking velocity in case of elastic collision. One may observe that the maximum of the restitution coefficient, as well as the minimum impact velocity necessary for the bounce to happen, increases as v_s' does. Indeed the higher v_s' the greater the kinetic energy that the particle loses to break the surface contact. Therefore, for the same values of e_0, which depends only on v_i/v_y, the final restitution coefficient e decreases as v_s'/v_y increases. On the other hand, keeping v_y constant and for high values of v_i the influence of the adhesion forces disappears and the restitution coefficient becomes independent from v_s'.

It is now important to emphasize that both the present and original Thornton and Ning models are based upon the Johnson-Kendall-Roberts (JKR) theory [18] and strictly valid
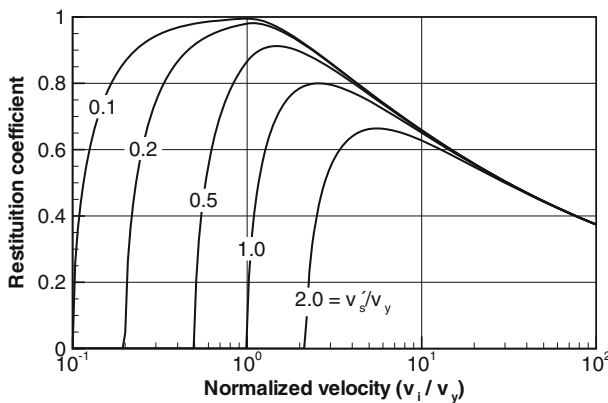

Fig. 2 Restitution coefficient as a function of the normalized normal impact velocity v_i/v_y for different values of v_s'/v_y

only for interactions occurring between solid particles and a smooth surface. Taking into account the adhesion force reduction due to the surface roughness is essential, not only for an accurate calculation of the sticking velocity but also for ensuring the effectiveness of the resuspension model [19]. Many authors, among whom Reeks et al. [20] deserve a mention, introduced stochastic models aiming at reproducing a random distribution of asperities on the surface linked with the actual rough surface adhesion energy distribution. In the present work a comprehensive reduction factor is utilized as proposed by Cheng et al. [21]. Accordingly, the reduction factor is assumed to be dependent on the statistical distribution in heights of the asperities and on the physical properties of the interface (e.g. equivalent Young's modulus and smooth-surface interface energy). That reduction can be easily seen as a reduction of the interface energy, introducing an equivalent interface energy for rough surfaces, given by:

$$\Gamma = C_a \, \Gamma_s \tag{18}$$

being C_a the reduction factor and Γ_s the interface energy for smooth surfaces.

Finally it is necessary to dwell on the evaluation of the interface energy and adhesion force for smooth surfaces. Since the first is not easily determinable unless by means of dedicated experiments, an estimate has been made following from the surface energies of the single materials in contact as suggested by Fuller and Tabor [22]:

$$\Gamma_s = \gamma_1 + \gamma_2 - \left(\sqrt{\gamma_1} - \sqrt{\gamma_2}\right)^2 . \tag{19}$$

2.4 Particle resuspension

Concerning the particle resuspension, a dynamic model is implemented. Dynamic models provide a description of particle motion on the wall with particular regard to the interaction between the particle motion and the wall asperities. As a matter of fact, although early models relied just on the balance between lift and adhesion forces exerted on the particles, it is now believed that particles preferentially start rolling or slipping on the wall [23] and then resuspend after crashing into an asperity with a proper energy. Tracking the motion of every particle (on the wall and within the fluid) brings a great improvement in the accuracy of the resuspension model, since it influences the coupling with the fluid and a particle may encounter a succession of resuspensions and depositions.

In order to properly characterize the resuspension phenomenon, the choice of the surface roughness description is essential. In the present model two scales of asperity heights are considered as shown in Fig. 3. The largest scale, of the same order of magnitude as the typical particle diameter (here micrometers), is considered as resuspension trigger, whereas the smallest scale, of the order of nanometers, is taken into account for the calculation of

Fig. 3 Representation of the surface roughness, consisting in hemispherical asperities of two different scales
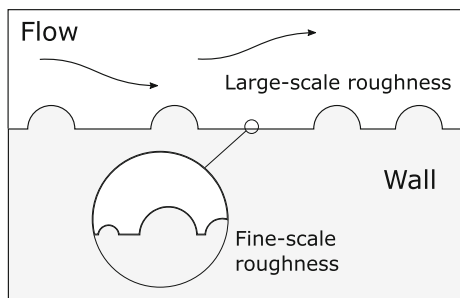
the rough-surface adhesion force, as shown in the following. The asperities are modeled as hemispherical and the large-scale ones have all the same height H_l. Provided that they are randomly distributed on the surface, it is assumed that the longitudinal distance between the asperities has a random distribution as well. It is also assumed that it may be approximated with a Poisson's law distribution, as random points uniformly distributed on an interval [24]. Namely the probability of finding n asperities traveling a distance of x on the wall is given by:

$$P(x, n) = \frac{1}{n!} \left(\frac{x}{L_l} \right)^n \exp\left(-\frac{x}{L_l} \right) \tag{20}$$

with L_l the mean distance between the asperities.

In order to derive the equation for the particle motion on the wall, evaluating the efforts exerted on them is needed. As sketched in Fig. 4, they are aerodynamic (drag and lift), adhesion and friction forces. The adhesion force F_a is computed in agreement with the JKR theory [18], taking into account the aforementioned correction for rough surfaces:

$$F_a = \frac{3}{4} \pi \Gamma d_p \tag{21}$$

with Γ the particle-wall interface energy. The contact radius a is given by:

$$a = \left(\frac{3\pi \Gamma_s d_p^2}{8K} \right)^{1/3} \tag{22}$$

with K the composite Young's modulus, which depends on the Young's moduli E_1 and E_2 and on the Poisson's ratios ν_1 and ν_2 of particle and wall, respectively:

$$K = \frac{4}{3} \left(\frac{1 - \nu_1^2}{E_1} + \frac{1 - \nu_2^2}{E_2} \right)^{-1}. \tag{23}$$

The drag force F_D is modeled as Stokesian, considering both the slip [25] and the wall [26] effects:

$$F_D = \left(3\pi \mu_f d_p V_{rel} \right) f / C_s \tag{24}$$

with $f = 1.7009$ the wall correction factor, C_s the slip correction factor and μ_f the dynamic viscosity of the fluid. The slip correction factor C_s is given by:

$$C_s = 1 + \frac{2l}{d_p} \left(A_1 + A_2 \exp \frac{-A_3 d_p}{l} \right) \tag{25}$$

Fig. 4 Sketch of the forces acting on a particle deposited at the wall and embedded within a flowing fluid
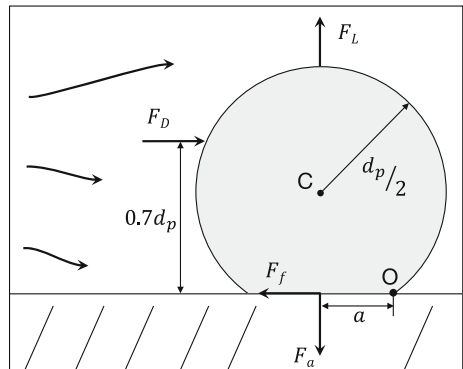
where $A_1 = 1.275$, $A_2 = 0.400$ and $A_3 = 0.55$ are constants and l is the mean free path of the fluid, given to a good approximation by:

$$l = \nu_f \sqrt{\frac{\pi}{2RT_f}} \tag{26}$$

with ν_f the kinematic viscosity of the fluid, T_f the absolute temperature and R the specific gas constant.

As for the particle transport within the fluid, the lift force F_L is computed by means of Eq. 6 where I_L takes the form of

$$I_L = 1.7438 - 5.5628\Lambda_g + 1.9811\Lambda_g^2 \tag{27}$$

for non-rotating particles and of

$$I_L = 1.780663 - 6.28059\Lambda_g + 1.768275\Lambda_g^2 \tag{28}$$

otherwise.

The friction force F_f is computed by means of the static and dynamic friction coefficients k_s and k_d. Where the particle-wall contact point velocity is greater than zero, F_f is given by:

$$F_f = k_d (F_a - F_L) \tag{29}$$

otherwise:

$$F_f = \min[k_s (F_a - F_L), F_D]. \tag{30}$$

For a motionless particle attached to the wall, three detachment methods or conditions are individuated [3]:

– Direct lift-off, where the lift overcomes the adhesion force:

$$F_L > F_a. \tag{31}$$

– Slipping, where the drag is greater than the friction force:

$$F_D > k_s (F_a - F_L). \tag{32}$$

– Rolling, where the moment of aerodynamic forces at point O is greater than the moment of the adhesion force:

$$(0.7d_p) F_D + aF_L > aF_a. \tag{33}$$

After a particle starts slipping or rolling on the wall, its position and velocity is computed by integrating the following equations, derived from the Newton's second law of motion:

$$m_p \frac{d\boldsymbol{v}}{dt} = \boldsymbol{F}_D + \boldsymbol{F}_L + \boldsymbol{F}_a + \boldsymbol{F}_f + \boldsymbol{\omega} \times \mathbf{OC}$$
$$I_p \frac{d\boldsymbol{\omega}}{dt} = \mathcal{M}_O(\boldsymbol{F}_D) + \mathcal{M}_O(\boldsymbol{F}_L) + \mathcal{M}_O(\boldsymbol{F}_a) \tag{34}$$

with m_p and I_p the mass and moment of inertia of the particle, $\boldsymbol{v}$ and $\boldsymbol{\omega}$ the linear and angular velocity. $\mathcal{M}_O(\boldsymbol{F})$ indicates the moment of a generic force $\boldsymbol{F}$ at point O. If a particle is directly lifted-off, Eq. 1 applies.

The adopted resuspension scheme assumes that a particle moving on the wall resuspends either by direct lift-off or when it crashes into a large-scale asperity, having a kinetic energy greater than the potential of adhesive forces. The particle-asperity collision condition is met where a drawn random number ξ is lower than the probability for a particle of finding at least one asperity during its travel. That probability is computed at each time step according to Eq. 20 as follows:

$$\xi < 1 - \exp\left(-\frac{\Delta s}{L_l}\right) \tag{35}$$

where L_l is the average distance between asperities and Δs the distance traveled by the particle on the wall during a generic time step. The energy condition is satisfied where:

$$E_k = \frac{1}{2} m_p \boldsymbol{v}^2 > V_A \tag{36}$$

with E_k the kinetic energy of the particle and V_A the Van der Waals interaction potential between the particle and the struck asperity, which is given by:

$$V_A = \frac{3}{4} \pi \Gamma d_p z_0 \tag{37}$$

where $z_0 \simeq 0.3$ nm is the contact distance, which corresponds to an atomic diameter. In case the resuspension occurs, a particle is re-entrained within the fluid with a velocity tangent to the particle-asperity contact point and whose projection on the xz plane is parallel to the particle velocity before the collision (Fig. 5). The new velocity magnitude v_1 is computed as:

$$v_1 = v_0 - \sqrt{\frac{2V_A}{m_p}} \tag{38}$$

being v_0 the particle velocity magnitude before the resuspension. In case the asperity is struck with insufficient kinetic energy to trigger a resuspension, the particle continues its motion on the wall where its energy is sufficient to climb over the asperity, namely:

$$E_k > m_p g H_l \tag{39}$$

with g the gravitational acceleration in the direction normal to the wall and H_l the asperity height. If the condition in Eq. 39 is not met, the particle is considered attached again to the wall, and its velocity is set to zero.

It is worth noting that the resuspension algorithm here introduced benefits of a lower computational cost in comparison with the one presented by Guingo and Minier [6] because of the stronger stochastic approach adopted in modeling the asperity-particle interactions.

3 Computational Details

A round jet originating from a perforated wall and impinging on a second wall parallel to the first one is here computed by means of the in-house finite differences Fortran code developed at the CFD Group of TU Berlin. The orifice has a diameter D of 3 mm, whereas the computational domain has a size of $12D \times 5D \times 12D$. A sketch of the domain containing

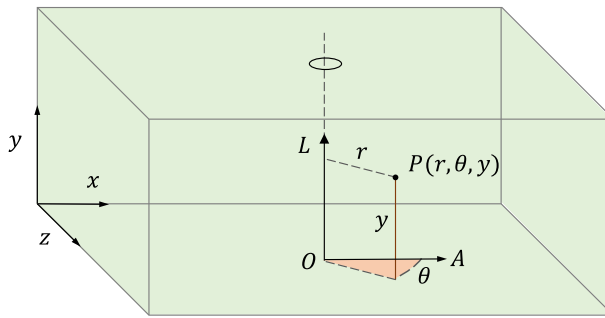**Fig. 5** Velocity before and after the particle-asperity contact, when a resuspension occurs
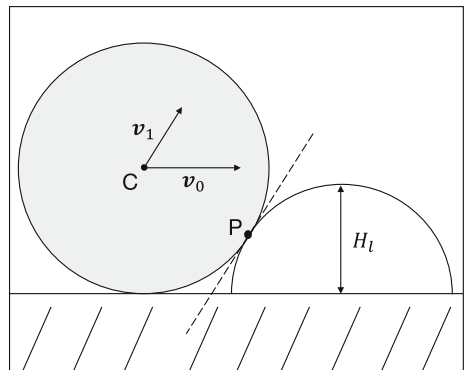
Fig. 6 Computational domain with the adopted Cartesian (x, y, z) and cylindrical (r, θ, y) coordinate systems. The latter is defined by the origin O, the polar axis A and the longitudinal axis L, which corresponds to the jet axis

the definition of the coordinate systems adopted in this paper is shown in Fig. 6. Since the dimensionless wall distance y^+ and the Kolmogorov length scale are not believed to be strongly influenced by the particles, the validity of the present DNS study is provided by adopting the same grid of 512 points in each direction utilized by Wilke and Sesterhenn [27] who successfully simulated the analogous flow in the absence of particles. Accordingly, the grid is refined in order to ensure a maximum value of y^+ at the closest grid points to the walls less than one. A grid stretching is also applied in the x and z directions to refine the mesh around the jet axis. The stretching functions, derived from the sine function for the y direction and from the hyperbolic tangent otherwise, lead to a maximum spacing variation respectively of 0.87% and 0.42% in the region with $r/D < 5$, with r the distance from the jet axis.

The main direction of the flow, whose definition is required for the computation of the lift force acting on the particles, is assumed to be radial (see Section 2). This is possible because the motion of particles, as shown in the following, is entirely confined within a small region ($y/D < 0.5$) near the lower wall.

In addition to the particle-wall interaction scheme described in the previous section, the adopted initial and boundary conditions are illustrated in the following for both the continuous and dispersed phases.

3.1 Continuous phase

The initial pressure and temperature of the fluid are set to 49.5 mbar and 373 K respectively. The temperature of the walls is kept constant to 373 K, whereas the jet bulk temperature is set to 293 K. The jet bulk velocity U_b is chosen to ensure, along with the temperature, a bulk Mach number equal to 1 so that a Reynolds number (based on the bulk velocity U_b and the inlet diameter D) of 3300 is computed. The velocity profile of the jet at the inlet is laminar and shaped in order to obtain a higher velocity at the edges than at the center of the jet, so that the *vena contracta* effect, which occurs when a fluid is forced through a sharp-edged orifice, is taken into account (see Fig. 7). Moreover the stationary velocity profile at the inlet is reached after a transient time t_s, approximately equal to half the time taken by the jet to reach the wall. The transient is realized with a scaling function, represented in Fig. 7, which multiplies the steady-state inlet velocity. The inlet temperature follows the same trend of the velocity profile with the prescribed bulk value. The velocity and temperature profiles also
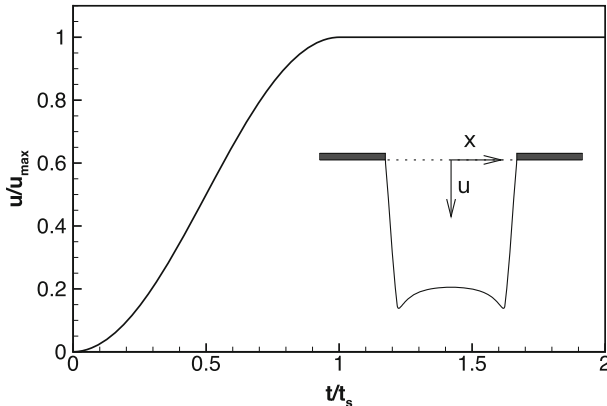
Fig. 7 Inlet velocity profile and scaling function of the inlet velocity profile against the dimensionless time t/t_s, with t_s the transient duration

implement a disturbed thin laminar annular shear layer in order to accelerate the turbulent transition.

The four x- and z-normal boundaries are set to be non-reflective. Furthermore, in order to destroy and absorb the vortices which are leaving the domain at the outlet, a sponge region is set for $r/D > 5$. That is realized by adding forcing terms, proportional to the difference between the computed quantities and reference values, to the right-hand side of the fluid transport equations. The reference values are taken from a previous LES carried out on a wider domain, extended in the x and z directions. It is worth underlining that the fluid and particle data in the sponge region are not taken into account nor showed as a result. To gain a better insight into the definition of the boundary conditions, reference is made to Wilke and Sesterhenn [28].

3.2 Dispersed phase

With regard to the particle initial conditions, the deposit is initialized on the lower wall by uniformly distributing particles within a circular area of radius $5D$. The particle diameters are assumed to be underlain by a log-normal distribution and randomly initialized using the inverse transform sampling method. The location and scale parameters of the distribution are respectively given by:

$$\mu = \ln(\text{CMD}) \quad \text{and} \quad \sigma = \ln(\text{GSD}) \tag{40}$$

where CMD indicates the count median diameter and GSD the geometric standard deviation of the diameters. Those parameters are chosen in accordance with the experimental evidence of Sharpe et al. [7] for the material eroded in the vacuum vessel of a representative prototype of fusion reactor (ASDEX-Upgrade facility, lower regions), i.e. CMD and GSD are set equal to 2.21 μm and 2.93 respectively. Furthermore, the distribution is slightly bounded above and below, in order to keep the typical particle diameter to asperity height ratio around 1 (see Section 2.4). The resulting probability density function (unbounded) is shown in Fig. 8.

The other particle properties (i.e. density, Young's module, Poisson's ratio, yield strength and surface energy) are constant for every particle and equal to the mass weighted averaged properties of the materials characterized in the same facility [29]. Accordingly, the composition 67.6 wt% Cu, 23.7 wt% Fe, 5.1 wt% Cr, and 3.6 wt% Ni is assumed. The resulting
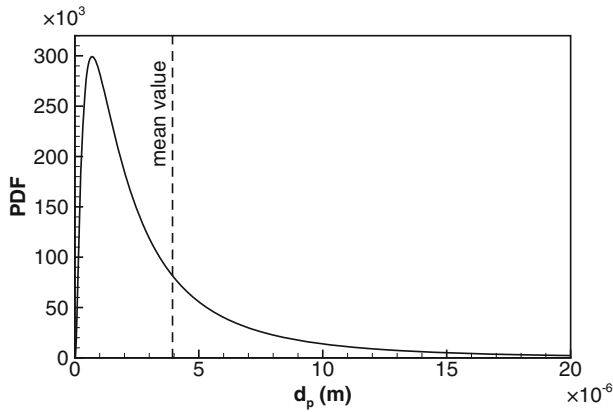
Fig. 8 Probability density function of the particle diameters

averaged properties are summarized in Table 1. The properties of copper are chosen for the wall, as its alloys are commonly used as vessel internal shield materials. Therefore the wall surface energy, Young's module and Poisson's ratio are set equal to 2.2 J/m^2, 117 GPa and 0.34 respectively, whereas 0.6 and 0.4 are chosen as static and dynamic friction coefficients. The large-scale asperities are assumed to have a height of 6.3 μm and an average distance of 30 μm. The smooth to rough adhesion force ratio C_a is set to 0.01 [21]. In consequence of the above assumptions and imposing an initial surface density of 12.3 g/m^2, a total number of about 10^7 particles corresponding to a total mass of 11.2 mg are initially dispersed on the wall.

4 Results and Discussion

In this section the simulation results are presented and discussed with reference to fluid and particles. An overall time of 0.88 ms (which corresponds to about 20 times as long as the jet takes to cover the space between the nozzle and the wall) has been simulated. The presented data are referred either by a Cartesian (x, y, z) or a cylindrical coordinate system (r, θ, y) as shown in Fig. 6.

Table 1 Properties and mass weighted average properties of the metal dust collected from ASDEX-Upgrade facility [29]

	Mass fraction (%)	Density (kg/m^3)	Young's module (GPa)	Poisson's ratio	Yield strength (MPa)	Surface energy (J/m^2)
Copper (Cu)	67.6	8890	117	0.34	70	1.83
Iron (Fe)	23.7	7780	210	0.23	130	2.48
Chrome (Cr)	5.1	7140	140	0.21	225	2.3
Nickel (Ni)	3.6	8600	170	0.31	245	2.45
Average		8527	142	0.31	98	2.03

Fig. 9 Fluid velocity magnitude contours on a plane passing through the jet axis at $t = 0.768$ ms. Time animation of this figure is available in Online Resource 1
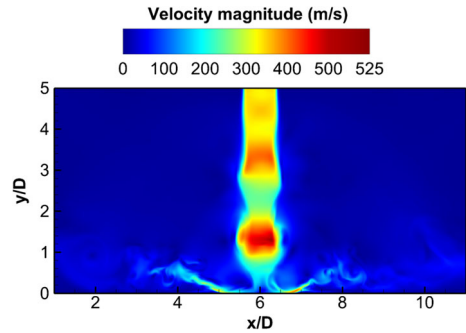
    Given the transient nature of the phenomenon, two characteristic time instants have been individuated by analyzing the velocity magnitude of the flow. A representative snapshot on a plane passing through the jet axis is shown in Fig. 9. Notably, the jet impacts on the wall at $t \simeq 0.124$ ms and the flow symmetry is broken at $t \simeq 0.313$ ms. Figure 10 shows the temperature contours on the same plane and the Nusselt number[2] Nu on the wall at two different time instants. It can be seen that the flow is highly unsteady and Nu varies from negative to positive, even thought its time average, taken in similar cases by Wilke and Sesterhenn [27], is positive all over the wall. Wilke and Sesterhenn additionally observed an inflection point of the average Nu curve at $r/D = 1.2$, where, according to the authors, secondary vortices originate, as inheritance of the Kelvin-Helmholtz instabilities (primary vortices) which appear in the shear layer of the free jet region. Figure 11 shows the time signal of the wall Nusselt number averaged over a circumference of radius $1.2D$; the two dashed vertical lines represent the jet impact and symmetry break instants, respectively. It is worth noting that the oscillations of the represented signal appear to be damped after the symmetry break. We mention this behavior as it becomes clear later that the same vortices which cause the elevated Nusselt number give rise to the particle resuspension.

    The number and total mass of resuspended and detached particles (as detached are indicated the particles in motion on the wall, but not resuspended) is shown in Figs. 12 and 13 as a function of time. One may see that the number of resuspended particles increases mostly in $t < 0.3$, whilst subsequently it grows almost linearly. In the same way, the total mass of resuspended particles grows mostly after the jet impact, but it does not any longer significantly increase for $t > 0.6$. Hence, it may be concluded that the large particles are resuspended faster than the small ones. It may be also observed that, unlike the mass and number of resuspended particles, both the mass and number of detached particles oscillate. This indicates that particles repeatedly attach to the wall and detach from it. Taking the FFT of the total detached mass and of the average Nusselt number at $r/D = 1.2$ (Fig. 14), it may be seen that, excluding the lowest frequencies, a peak occurs at St $\simeq 0.35$ (the Strouhal number St is defined as fD/U_b, with f the frequency) in both the transforms. That behavior can be explained considering that the secondary vortices repeatedly brush the wall with a characteristic frequency, conditioning both the heat exchange (Nusselt number) and particle motion.

_____

[2]Being computed as the non-dimensional wall normal derivative of the temperature, the Nusselt number quantifies the heat transfer at the impinging plate.
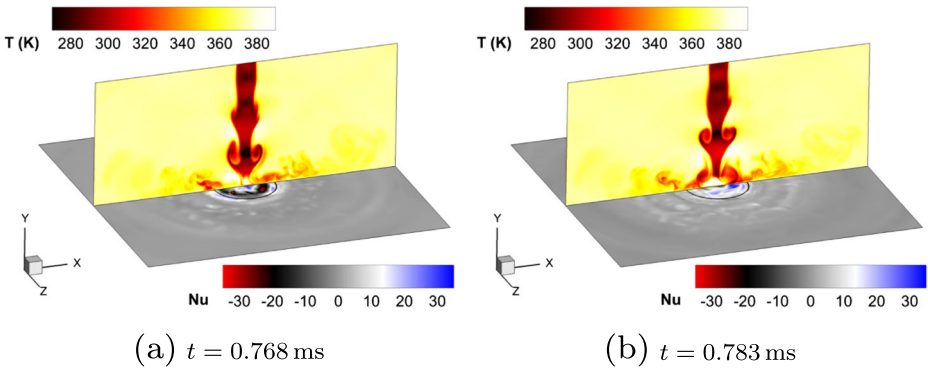
(a) $t = 0.768\,\text{ms}$ (b) $t = 0.783\,\text{ms}$

Fig. 10 Temperature contours on a plane passing through the jet axis and Nusselt number contours at the lower wall. The black circumference on the wall represents $r/D = 1.2$. Time animation of this figure is available in Online Resource 2

Figure 15 shows the deposit surface density and local CMD at $t = 0.88\,\text{ms}$. It may be observed that the jet interaction with the deposit becomes negligible for $r/D > 1$. Major effects occur in $r/D < 0.5$, where the density reaches minimum values lower than 1 g/m^2. Also the local CMD becomes about one third of the initial value in the area where the majority of resuspensions occurs.

Figure 16 reports the positions of 10% of the resuspended particles, randomly sampled and colored by their diameter and velocity (note that the y scale ranges between 0 and $0.5D$); on the background the fluid velocity magnitude is contoured using a grayscale color map. It may be seen that at first the large particles tend to resuspend quicker than the small ones. Subsequently, the former stratify and trail the vortex rising upwards, whereas the latter, which are increasingly accelerated, travel faster to the outlet following a radial direction. By comparing the figures, it may be observed that the particle velocity is roughly independent on their diameter, whereas a strong influence should be ascribed to the carrier fluid velocity and, thus, to the particle positions within the flow.

Three typologies of particle-fluid-wall interactions have been statistically investigated: resuspensions, detachment from the wall (excluding resuspensions) and particle-wall
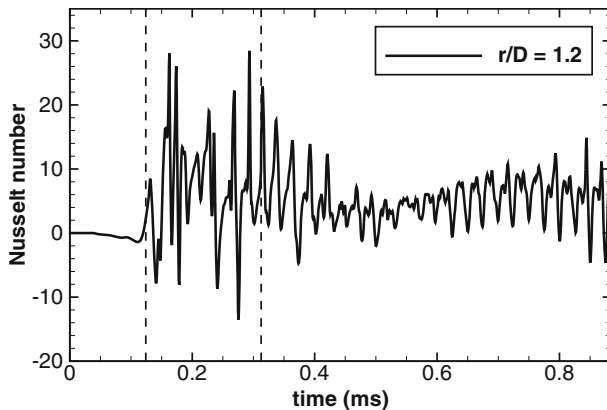

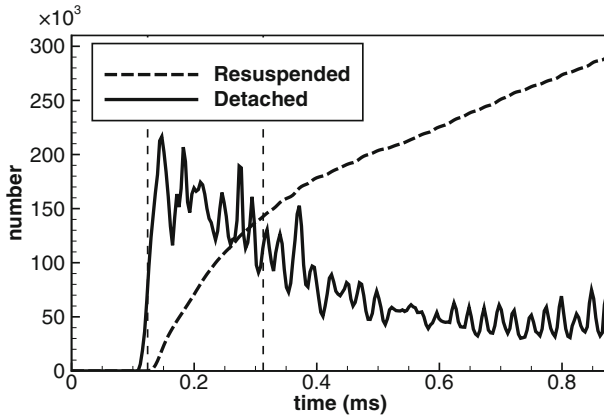**Fig. 11** θ-averaged Nusselt number at $r/D = 1.2$ vs. time

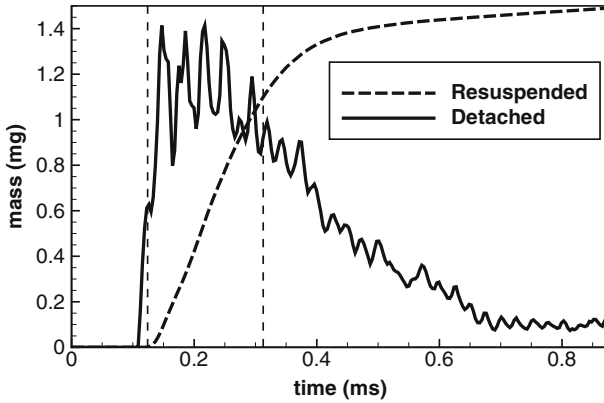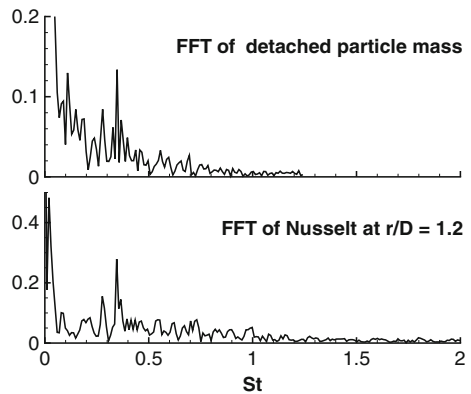**Fig. 12** Number of detached and resuspended particles vs. time

Fig. 13 Mass of detached and resuspended particles vs. time

Fig. 14 FFTs of the Nusselt
number at $r/D = 1.2$ and of the
total detached particle mass. Both
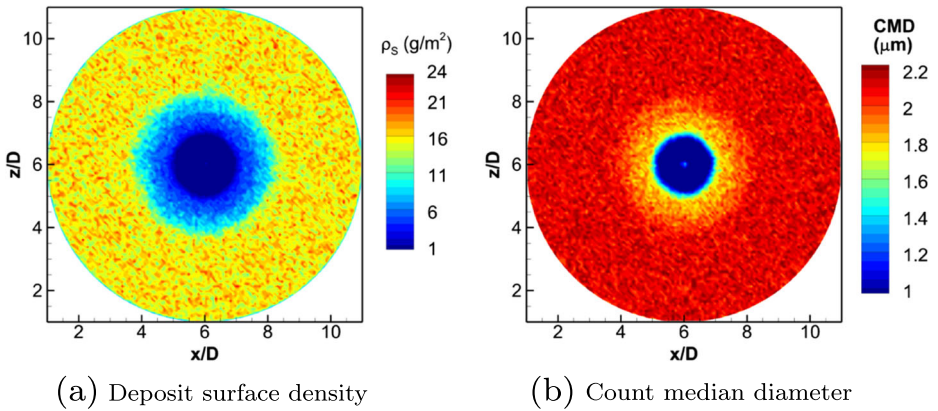the transforms are normalized
with their respective maxima

(a) Deposit surface density

(b) Count median diameter

Fig. 15 Local deposit properties at $t = 0.88$ ms. Time animation of this figure is available in Online Resource 3

impacts occurring to the particles which have been already resuspended. By analyzing Table 2, it may be noted that the CMD of resuspended particles is about 5.88 μm (whereas the deposit initial CMD is 2.21 μm) and 93% of the deposited particle mass is resuspended in $r/D < 1.5$. Moreover, it may be noted that each detached particle is typically re-attached
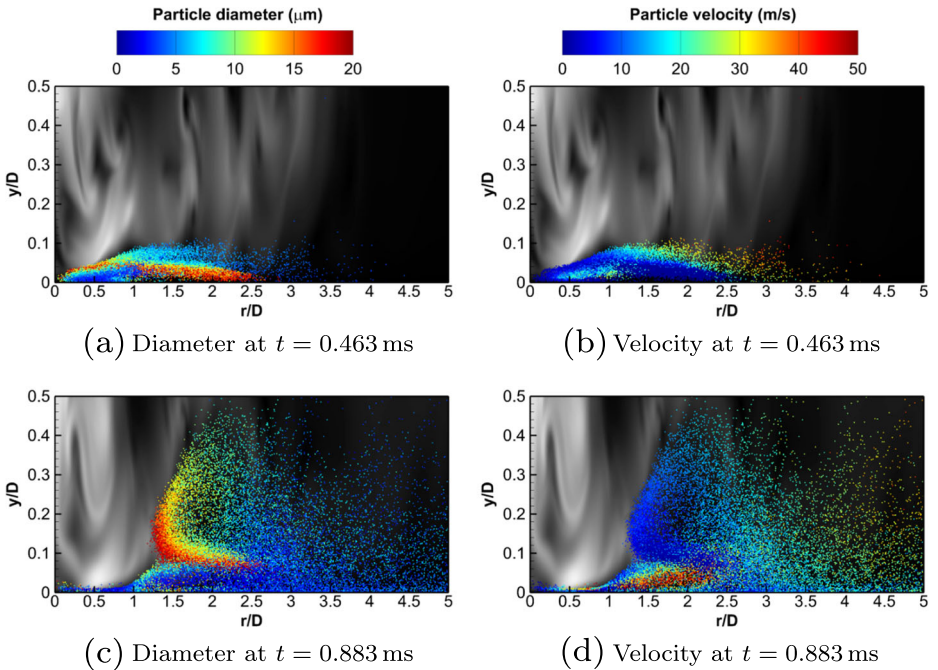

(a) Diameter at $t = 0.463$ ms

(b) Velocity at $t = 0.463$ ms

(c) Diameter at $t = 0.883$ ms

(d) Velocity at $t = 0.883$ ms

Fig. 16 Position of 10% of the resuspended particles at different times. The particles shown are randomly sampled and colored by their diameter and velocity. It should be noted that the aspect ratio of the plot is deliberately distorted to improve the readability of the results. Time animation of this figure is available in Online Resources 4 and 5

Table 2 Summary of the particle-fluid-wall interaction statistics

Resuspensions	CMD	5.88 μm
	Number	291,110
	Total mass	1.49 mg
	Fraction of resuspended particles	
	whole domain	2.8%
	$r/D < 1.5$	37.8%
	Mass fraction of resuspended particles	
	whole domain	13.3%
	$r/D < 1.5$	93.1%
Detachments	CMD	5.79 μm
	Number	7,731,508
	Number of particles that detach at least once	840,569
	Average number of detachments per detached particle	9.2
Impacts	CMD	3.78 μm
	Number	18,137
	whereof deposits	43
	Average normal impact velocity	1.28 m/s
	Average restitution coefficient	0.196

and then re-detached on the average for 9.2 times during the simulation. It has also been found that the average travel on the wall of a generic particle before being resuspended is about 3.31 times its own diameter and 3.85 times the deposit initial CMD. The vast majority of the particle motions on the wall is simple rolling.

Figure 17 shows the probability density functions of the interactions. The distribution of detachments has a greater variance than the distribution of resuspensions, since detachments occur more uniformly and in a wider region around the jet axis. The large majority of the resuspensions and detachments take place within $r/D < 1$, even though they are mostly condensed in an annulus with $0.3 < r/D < 0.8$. The PDF of the impacts shows that impact occurrences are more irregularly scattered and the distribution does not appear to follow a marked pattern.
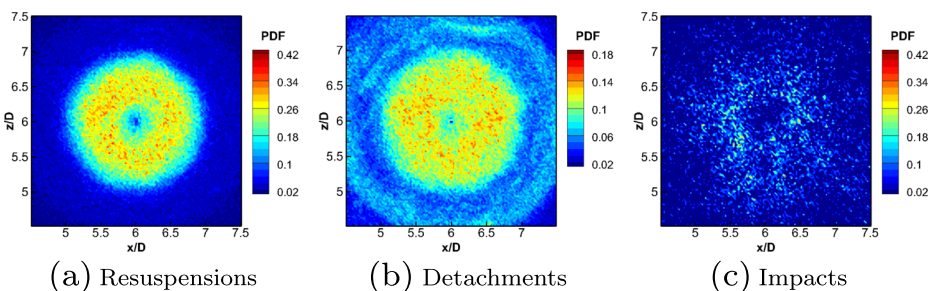

(a) Resuspensions　　　　　(b) Detachments　　　　　(c) Impacts

Fig. 17 Probability density functions of the resuspension, detachment and impact occurrences

Finally, it should be noted that particle mass and volume fraction in the fluid are always lower than $1.4 \cdot 10^{-4}$ and $8 \cdot 10^{-10}$, respectively. Since those are much lower than the commonly accepted threshold values above which particle-particle collisions should be considered (for instance, see [12]), the validity of the two-way coupling approach can be ensured.

5 Conclusions

In this paper a DNS of a multiphase transonic impinging jet flow has been presented, placing particular emphasis on the interaction between jet and micrometer scale solid spherical particles deposited on the impingement wall, i.e. resuspensions, detachments and impacts. Being those phenomena of crucial interest in the safety assessment of nuclear fusion power plants, the flow occurring during a Loss Of Vacuum Accident (LOVA) has been reproduced. The main achievements can be summarized as follows:

– Resuspensions and detachments mostly occur in a circular region of radius approximately equal to 1 jet diameter. Particularly, the majority of resuspensions takes place in an annulus of radii from 0.3 to 0.8 diameters, since the interactions reduce in the stagnation region. Impact occurrences do not appear to condense in any particular region or to follow a distinct pattern.
– The vast majority of the particle motions on the wall is simple rolling, in other words detachments for slipping are negligible. On the other hand, although most of the resuspensions take place as a consequence of the particle-wall asperity collision, 6.5% of them are direct resuspensions, i.e. the lift force alone suffices to break the particle-wall contact.
– The probability of a generic particle to be resuspended after its detachment is only 3.77%.
– The larger a particle, the higher is the probability to find it detached and later resuspended. Hence, the larger particles resuspend faster. As a consequence, it has been observed that during the first instants after the jet impingement, the total resuspended mass increases more rapidly than the resuspended particle number. At a later stage, the removed mass remains roughly constant whereas the resuspended particle number increases approximately linearly.
– The motion of particles on the wall is highly unsteady, as it follows the generation and destruction of wall vortices. Indeed, it has been found that particles repeatedly detach, roll and reattach with a period compatible with that of the secondary vorticity formation at the wall.

Despite the remarkable modeling effort made for this work, further advances in the present resuspension model remain to be achieved. For instance, particle-particle interactions, such as cohesion, break-up and collision, as well as electrostatic effects shall be addressed in the future (using the same approach, for example, presented in the recent work by Almohammed and Breuer [30]). Of interest and deserving of being additionally investigated is also the role played by strong shocks in the phenomenon. As a matter of fact, strong shocks are expected to occur for higher Mach numbers, which might presumably appear, for instance, during a LOVA in a fusion reactor. Additionally, the assumption by which some particle properties are kept constant is worth to be removed, since most of the particulate that can be found in nature or industry is likely composed of several materials.

Compliance with Ethical Standards

Conflict of interests   The authors declare that they do not have any conflict of interest in the authorship or publication of this contribution.

References

1. Henry, C., Minier, J.P.: Progress in particle resuspension from rough surfaces by turbulent flows. Prog. Energy Combust. Sci. **45**, 1–53 (2014)
2. Cleaver, J., Yates, B.: Mechanism of detachment of colloidal particles from a flat substrate in a turbulent flow. J. Colloid Interface Sci. **44**(3), 464–474 (1973)
3. Ibrahim, A., Dunn, P., Brach, R.: Microparticle detachment from surfaces exposed to turbulent air flow: controlled experiments and modeling. J. Aerosol Sci. **34**(6), 765–782 (2003)
4. Ibrahim, A., Dunn, P., Qazi, M.: Experiments and validation of a model for microparticle detachment from a surface by turbulent air flow. J. Aerosol Sci. **39**(8), 645–656 (2008)
5. Reeks, M., Hall, D.: Kinetic models for particle resuspension in turbulent flows: theory and measurement. J. Aerosol Sci. **32**(1), 1–31 (2001)
6. Guingo, M., Minier, J.P.: A new model for the simulation of particle resuspension by turbulent flows based on a stochastic description of wall roughness and adhesion forces. J. Aerosol Sci. **39**(11), 957–973 (2008)
7. Sharpe, J., Petti, D., Bartels, H.W.: A review of dust in fusion devices: Implications for safety and operational performance. Fusion Eng. Des. **63**, 153–163 (2002)
8. Gaudio, P., Malizia, A., Lupelli, I.: Experimental and numerical analysis of dust resuspension for supporting chemical and radiological risk assessment in a nuclear fusion device. In: Conference Proceedings-International Conference on Mathematical Models for Engineering Science (MMES'10), vol. 30, pp. 2010–30. Puerto De La Cruz (2010)
9. Ciparisse, J., Malizia, A., Poggi, L., Gelfusa, M., Murari, A., Mancini, A., Gaudio, P.: First 3d numerical simulations validated with experimental measurements during a lova reproduction inside the new facility stardust-upgrade. Fusion Eng. Des. **101**, 204–208 (2015)
10. Sesterhenn, J.: A characteristic-type formulation of the Navier–Stokes equations for high order upwind schemes. Comput. Fluids **30**(1), 37–67 (2000)
11. Bogey, C., De Cacqueray, N., Bailly, C.: A shock-capturing methodology based on adaptive spatial filtering for high-order non-linear computations. J. Comput. Phys. **228**(5), 1447–1465 (2009)
12. Elghobashi, S.: On predicting particle-laden turbulent flows. Appl. Sci. Res. **52**(4), 309–329 (1994)
13. Morrison, F.: An Introduction to Fluid Mechanics Cambridge University Press (2013)
14. Schiller, L., Naumann, A.: Über die grundlegenden Berechnungen bei der Schwerkraftaufbereitung. Ver. Deut. Ing. **77**, 318–320 (1933)
15. Cherukat, P., McLaughlin, J.B.: The inertial lift on a rigid sphere in a linear shear flow field near a flat wall. J. Fluid Mech. **263**, 1–18 (1994)
16. Thornton, C., Ning, Z.: A theoretical model for the stick/bounce behaviour of adhesive, elastic-plastic spheres. Powder Technol. **99**(2), 154–162 (1998)
17. Wu, C.Y., Li, L.Y., Thornton, C.: Rebound behaviour of spheres for plastic impacts. Int. J. Impact Eng. **28**(9), 929–946 (2003)
18. Johnson, K., Kendall, K., Roberts, A.: Surface energy and the contact of elastic solids. In: Proceedings of the Royal Society of London A: Mathematical, Physical and Engineering Sciences, vol. 324, pp. 301–313. The Royal Society (1971)
19. Greenwood, J., Williamson, J.: Contact of nominally flat surfaces. In: Proceedings of the Royal Society of London A: Mathematical, Physical and Engineering Sciences, vol. 295, pp. 300–319. The Royal Society (1966)

20. Reeks, M., Reed, J., Hall, D.: On the resuspension of small particles by a turbulent flow. J. Phys. **21**(4), 574 (1988)
21. Cheng, W., Dunn, P., Brach, R.: Surface roughness effects on microparticle adhesion. J. Adhesion **78**(11), 929–965 (2002)
22. Fuller, K., Tabor, D.: The effect of surface roughness on the adhesion of elastic solids. In: Proceedings of the Royal Society of London A: Mathematical, Physical and Engineering Sciences, vol. 345, pp. 327–342. The Royal Society (1975)
23. Ziskind, G., Fichman, M., Gutfinger, C.: Resuspension of particulates from surfaces to turbulent flows— review and analysis. J. Aerosol Sci. **26**(4), 613–644 (1995)
24. Papoulis, A.: Probability, Random Variables, and Stochastic Processes. Communications and Signal Processing. McGraw-Hill (1991)
25. O'Neill, M.: A sphere in contact with a plane wall in a slow linear shear flow. Chem. Eng. Sci. **23**(11), 1293–1298 (1968)
26. Friedlander, S.K.: Smoke, Dust and Haze: Fundamentals of Aerosol Behavior. Wiley-Interscience, New York (1977)
27. Wilke, R., Sesterhenn, J.: Statistics of fully turbulent impinging jets. J. Fluid Mech. **825**, 795–824 (2017)
28. Wilke, R., Sesterhenn, J.: Direct numerical simulation of heat transfer of a round subsonic impinging jet. In: Active Flow and Combustion Control 2014, pp. 147–159. Springer (2015)
29. Sharpe, J.P., Rohde, V., Team, T.A.U.E., Sagara, A., Suzuki, H., Komori, A., Motojima, O., Group, T.L.E.: Characterization of dust collected from Asdex-Upgrade and LHD. J. Nucl. Mater. **313**, 455–459 (2003)
30. Almohammed, N., Breuer, M.: Modeling and simulation of particle–wall adhesion of aerosol particles in particle-laden turbulent flows. Int. J. Multiph. Flow **85**, 142–156